Anisotropy in the dielectric function of Bi₂Te₃ from first principles: From the UV-visible to the infrared range

R. Busselez¹, A. Levchuk¹, P. Ruello¹, V. Juvé¹ and B. Arnaud¹

¹ Institut des Molécules et Matériaux du Mans, UMR CNRS 6283,

Le Mans université, 72085 Le Mans, France, EU

(Dated: June 28, 2023)

Abstract

The dielectric properties of Bi₂Te₃, a layered compound crystallizing in a rhombohedral structure, are investigated by means of first-principles calculations at the random phase approximation level. A special attention is devoted to the anisotropy in the dielectric function and to the local field effects that strongly renormalize the optical properties in the UV-visible range when the electric field is polarized along the stacking axis. Furthermore, both the Born effective charges for each atom and the zone center phonon frequencies and eigenvectors needed to describe the dielectric response in the infrared range are computed. Our theoretical near-normal incidence reflectivity spectras in both the UV-visible and infrared range are in fairly good agreement with the experimental spectras, provided that the free carriers Drude contribution arising from defects is included in the infrared response. The anisotropic plasmon frequencies entering the Drude model are computed within the rigid band approximation, suggesting that a measurement of the reflectivity in the infrared range for both polarizations might allow to infer not only the type of doping but also the level of doping.

PACS numbers: 63.20.dk, 71.15.Mb, 78.20.-e, 78.30.-j, 78.40.-q

I. INTRODUCTION

A great deal of interest has been focused on Bi₂Te₃ because of its outstanding thermoelectric properties at room temperature arising from both a narrow gap electronic structure and a low thermal conductivity¹. The more recent discovery of three-dimensional topological insulators has renewed the interest for this compound. Indeed, soon after Bi₂Te₃ was theoretically predicted to host topologically non trivial metallic surface states with a Dirac-like dispersion around the surface Brillouin zone center², some angular-resolved photoemission spectroscopy (ARPES) studies revealed the existence of such linearly dispersing surface states³⁻⁵. While these extraordinary electronic properties encoded in the bulk wavefunctions have been thoroughly investigated both experimentally⁶⁻¹⁰ and theoretically¹¹⁻¹⁶, the infrared (IR) and optical responses have been studied more sparsely^{17–20}, notwithstanding the fact that applications in the technology relevant IR to visible range have been envisionned. Indeed, experiments have shown that Bi₂Te₃ can support surface plasmons in the entire visible range²¹ and some ellipsometry measurements even suggest that Bi₂Te₃ is a natural hyperbolic material in the near-IR to visible spectral range with appealing applications like hyperresolved superlensing²². Surprisingly, the optical properties inferred from reflectivity spectras 19 or ellipsometry measurements $^{20-22}$ are rather scattered. Hence, it's important to compute reference optical properties at a given level of theory²³ that can be directly compared to the available experimental results. Such a confrontation between theory and experiment is crucial not only to refine the level of theory needed to achieve a good description of the experimental results but also to spur new experiments guided by theory.

The paper is organized as follows. In section II, we give an account of the technicalities used to perform our first-principles calculations. In section III, we describe the crystal-lographic structure of Bi₂Te₃ and compare our calculated lattice constants and internal coordinates to the experimental values extracted from X-ray measurements. In section IV, we discuss the rather complex bandstructure including spin-orbit coupling (SOC) computed within the local density approximation (LDA) and show that the band gaps, as expected and already demonstrated in other theoretical studies^{13–16}, are underestimated with respect to the values infered from optical spectroscopy measurements. In section V, we compute the optical properties within the random phase approximation (RPA) for an electric field either parallel or perpendicular to the stacking axis, discuss the crucial role of local field

(LF) effects and make a direct comparison with available experimental results. In section VI, we compare our calculated zone center phonon frequencies to the frequencies extracted from both Raman and infrared (IR) spectroscopy measurements. In section VII, we compute the Born effective charge tensors that are key ingredients to compute the IR dielectric tensor. In section VIII, we derive the formalism used to compute the IR dielectric tensor with our home made code and discuss the anisotropy in our computed dielectric tensor for frequencies in the THz range. In section IX, we compute the normal incidence reflectivity spectras for both polarizations and only partially reproduce the experimental spectras because free carriers arising from defects contribute to the IR dielectric tensor and lead to a drastic change in the calculated spectras. Finally, in section X, we compute the anisotropic plasmon frequencies using a rigid band approximation for different type and level of doping. A direct comparison with the fitted plasmon frequencies used in part IX to reproduce the experimental spectras seems to indicate that it might be possible to infer not only the type of doping but also the level of doping from our calculations.

II. COMPUTATIONAL DETAILS

All the calculations are done within the framework of the local density approximation (LDA) for the exchange-correlation functional to density functional theory (DFT) using the ABINIT code^{24,25}. Relativistic separable dual-space Gaussian pseudo-potentials²⁶ are used with Bi $(6s^26p^3)$ and Te $(5s^25p^4)$ levels treated as valence states. Spin-orbit coupling is included and an energy cut-off of 40 Hartree in the planewave expansion of wavefunctions together with a $16 \times 16 \times 16$ kpoint grid for the Brillouin zone integration are used.

III. LATTICE PARAMETERS AND INTERNAL COORDINATES

 $\mathrm{Bi_{2}Te_{3}}$ crystallizes in a rhombohedral structure, also called A7 structure, with five atoms per unit cell. The vectors spanning the unit cell are given by

$$\mathbf{a}_1 = \left(a\xi, -\frac{a\xi}{\sqrt{3}}, h\right); \mathbf{a}_2 = \left(0, \frac{2a\xi}{\sqrt{3}}, h\right); \mathbf{a}_3 = \left(-a\xi, -\frac{a\xi}{\sqrt{3}}, h\right), \tag{1}$$

where $\xi = \sin\left[\frac{\alpha}{2}\right]$ and $h = a\sqrt{1 - \frac{4}{3}\xi^2}$. The length of the three lattice vectors is equal to a and the angle between any pair of vector is α . The three Te atoms can be classified into

TABLE I. Calculated LDA lattice parameters and internal parameters including spin-orbit coupling (SOC) compared to both existing experimental^{27,28} and theoretical¹² results.

| | Rhombohedral structure Hexagonal structure Internal parameters | | | | | | |
|-------------------|--|-------------------------|-----------------------|-------------------|------------|------------|--|
| | a_0 (Å) α_0 (°) | V_0 (Å ³) | $a_{\parallel,0}$ (Å) | $a_{\perp,0}$ (Å) | ν (Te) | μ (Bi) | |
| Expt. 27,28 | 10.473 24.159 | 169.10 | 30.487 | 4.383 | 0.2095 | 0.4001 | |
| This work (0 K) | 10.214 24.706 | 163.71 | 29.692 | 4.370 | 0.2071 | 0.4009 | |
| $LDA + SOC^{12}$ | 10.124 24.806 | 160.65 | 29.423 | 4.349 | 0.2063 | 0.4012 | |
| This work (300 K) | 10.473 24.159 | 169.10 | 30.487 | 4.383 | 0.2091 | 0.4002 | |

two inequivalent types. Two of them, labelled as Te_1 , are located at $\pm \nu \mathbf{c}$ while the last Te atom, labelled as Te_2 , is set at the origin. The two Bi atoms are equivalent and located at $\pm \mu \mathbf{c}$. Here ν and μ are dimensionless parameters and $\mathbf{c} = \mathbf{a}_1 + \mathbf{a}_2 + \mathbf{a}_3$ is parallel to the trigonal axis (C_3 axis). The rhombohedral structure is depicted in Fig. 1(a). Alternatively, the structure can be viewed as an hexagonal structure depicted in Fig. 1(b) and spanned by the following three lattice vectors

$$\mathbf{a}_{\perp,1} = \mathbf{a}_1 - \mathbf{a}_2; \ \mathbf{a}_{\perp,2} = \mathbf{a}_2 - \mathbf{a}_3; \ \mathbf{a}_{\parallel} = \mathbf{c},$$
 (2)

where $a_{\perp,1} = a_{\perp,2} \equiv a_{\perp}$. The lattice cell parameters of the two structures are related to each other by the following relations

$$a_{\perp} = 2a \sin\left(\frac{\alpha}{2}\right) \qquad a = \frac{1}{3}\sqrt{3a_{\perp}^2 + a_{\parallel}^2}$$

$$a_{\parallel} = a\sqrt{3 + 6\cos(\alpha)} \quad \sin\left[\frac{\alpha}{2}\right] = \frac{3}{2}a_{\perp}/\sqrt{3a_{\perp}^2 + a_{\parallel}^2}.$$
(3)

The hexagonal structure is easier to visualize as compared to the rhombohedral structure and can be viewed as made of three quintuple layers Te₁-Bi-Te₂-Bi-Te₁. However, it's worth noting that all the calculations have been performed using the rhombohedral structure because it contains three times atoms less than the hexagonal structure.

The calculated LDA lattice parameters including spin-orbit coupling (SOC) are displayed in table I and compared to the lattice parameters obtained from X-ray diffraction experiments performed at 300 K²⁷ as well as to other existing theoretical results¹². Our calculated lattice parameters $a_{\parallel,0}$ and $a_{\perp,0}$ are slightly larger than those obtained by Luo *et al*¹². Such a difference might be due to a different choice of the pseudo-potentials and/or to a different implementation of the electronic structure calculation. We also observe that our calculated

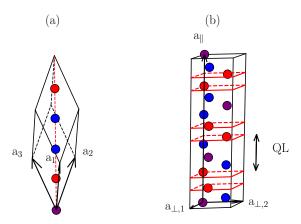


FIG. 1. (a) Rhombohedral structure with 5 atoms per unit cell. The two Te₁ atoms, the Te₂ atom and the two Bi atoms are respectively colored in red, purple and blue. (b) Hexagonal structure with 15 atoms per unit cell. The planes containing Te₁ atoms are highlighted and one quintuple layer (QL) Te₁-Bi-Te₂-Bi-Te₁ is shown.

 $a_{\parallel,0}$ and $a_{\perp,0}$ are respectively underestimated from 2.6 % and 0.3 % with respect to the experimental values²⁷. Such an underestimation for $a_{\parallel,0}$ might be ascribed to thermal expansion effects ignored in our calculations and to long range effects such as Van der Waals interactions not captured by the LDA exchange-correlation functional. It's worth considering the three relevant distances between successive planes perpendicular to the stacking axis (trigonal axis). When considering the fully relaxed structure, the two shortest distances $d_{Bi-Te_1} = 1.75$ Å and $d_{Bi-Te_2} = 2.0$ Å are in fairly good agreement with $d_{Bi-Te_1}^{expt} = 1.74$ Å and $d_{Bi-Te_2}^{expt} = 2.03$ Å whereas the largest distance $d_{Te_1-Te_1} = 2.40$ Å is strongly underestimated with respect to $d_{Te_1-Te_1}^{expt} = 2.61$ Å in accordance with the fact that Van der Waals interactions between Te₁ atoms are expected to be significant. In contrast, the interplane distances $d_{Bi-Te_1} = 1.75$ Å , $d_{Bi-Te_2} = 2.04$ Å and $d_{Te_1-Te_1} = 2.59$ Å are almost correctly predicted when imposing the experimental lattice parameters and relaxing the internal coor-

dinates μ and ν . All the forthcoming calculations have been performed for the experimental lattice parameters²⁷ and for the relaxed internal coordinates shown in table I.

IV. ELECTRONIC STRUCTURE AT THE LDA LEVEL

The electronic structure of Bi₂Te₃ has received a lot of attention and has been studied either at the DFT level^{11,12} or at the GW level^{13–16}. As shown in Fig. 2, the band structure, even at the LDA level, is rather complex. Indeed, the spin-orbit coupling (SOC) produces

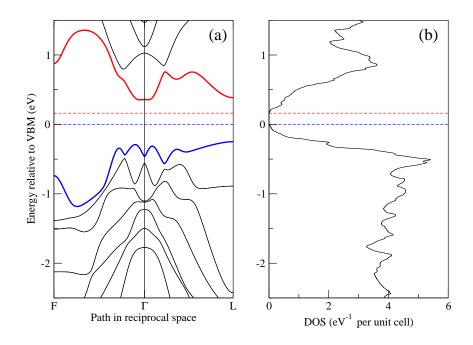


FIG. 2. (a) LDA bandstructure of Bi_2Te_3 including spin-orbit coupling (SOC) calculated along F- Γ -L where F = (0, 0.5, 0.5) and L = (0, 0.5, 0) in units of the reciprocal lattice vectors. The last valence bands and first conduction bands are respectively colored in blue and red. (b) Density of states (DOS) per unit cell computed for a $256 \times 256 \times 256$ grid of kpoints with a gaussian smearing of 10 meV. In both pannels, the valence band maximum is set at zero and displayed as a blue dashed line while the conduction band minimum is displayed as a red dashed line. The conduction bands are shifted towards higher energies from 120 meV to mimic the self-energy corrections.

a band inversion in the vicinity of the Γ point and shifts the band extremas from the high symmetry lines. Our calculated band extremas are found in the three mirror planes in agreement with other theoretical studies^{11–13,16}. As two extremas are found in each mirror plane, the multiplicity of our calculated extremas is 6 as suggested by Shubnikov-de Haas experiments^{6,7} and Landau level spectroscopy⁸. The extremas of the valence band and conduction band in the x=0 mirror plane depicted in Fig. 3 are respectively found at $\pm (0.349, 0.523, 0.349)$ and $\pm (0.542, 0.647, 0.542)$ in units of the reciprocal lattice vectors while these extremas are respectively located at $\pm (0.37, 0.54, 0.37)$ and $\pm (0.58, 0.68, 0.58)$ in Ref.¹³. Furthermore, the calculated LDA indirect gap is ~ 42 meV while the minimum direct

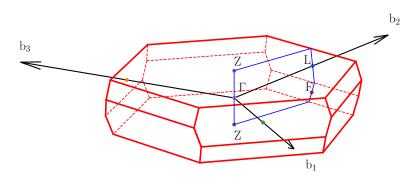


FIG. 3. First Brillouin zone where the x=0 mirror plane (in blue) has been highlighted and where four high symetry **k**-points, labelled Γ , Z, L and F are shown. The x=0 mirror plane is spanned by the reciprocal lattice vectors \mathbf{b}_2 ($\Gamma - L$ direction) and $\mathbf{b}_1 + \mathbf{b}_2 + \mathbf{b}_3$ ($\Gamma - Z$ direction) and the two other mirror planes (not shown) are obtained by applying C_3 rotations around the trigonal axis to the x=0 mirror plane.

gap is ~ 91 meV. The indirect gap differs from the LDA gap ~ 87 meV reported in Ref.¹³. Such a difference might be ascribed to the lattice cell parameters and/or internal coordinates that are expected to play a significant role on both the positions of the extremas and the values of the gaps¹⁶. Optical measurements performed at 10 K led to a probably indirect

band gap of $150 \pm 20 \text{ meV}^{29}$ and a direct gap of $220 \pm 20 \text{ meV}^{29}$ confirmed by more recent ellipsometry measurements²⁰. The discrepancy between the theoretical and experimental results is noticeable and reflects the fact that the LDA eigenvalues can not be interpreted as quasiparticle energies. More sophisticated approaches based on the evaluation of the selfenergy within the GW approximation^{23,30–32}, are needed to provide a better description of quasiparticle properties. All the GW calculations ^{13–16} produce band gaps in better agreement with experiments. It's worth highlighting that an accurate description of the quasiparticle bandstructure near the Γ point necessitates to take into account the non diagonal elements of the self-energy operator¹⁵. The self-energy corrections, while less than 200 meV for one band and one kpoint¹⁴, are highly non trivial. Indeed, the rigid shift scissor approximation is not valid for the highest valence band and lowest conduction band^{14,15}, especially in the vicinity of the Γ point where the band inversion occurs and where the direct LDA band gaps are reduced¹⁵. However, as this approximation seems to be well founded for other bands, we shift all conduction bands from 120 meV with respect to the valence bands to reproduce both the experimental indirect and direct gaps and keep in mind that we only achieve a poor description of the self-energy corrections needed to compute the optical properties beyond the standard random-phase approximation (RPA).

V. OPTICAL PROPERTIES AT THE RPA LEVEL

Within the RPA 33,34 , the dielectric matrix for a given \mathbf{q} wavevector reads:

$$\epsilon_{\mathbf{G},\mathbf{G}'}(\mathbf{q},\omega) = \delta_{\mathbf{G},\mathbf{G}'} - \frac{e^2}{4\pi\epsilon_0} \frac{4\pi}{v|\mathbf{q} + \mathbf{G}||\mathbf{q} + \mathbf{G}'|} \frac{1}{N} \sum_{\mathbf{k},n,m} \frac{f_{n,\mathbf{k}-\mathbf{q}} - f_{m,\mathbf{k}}}{\epsilon_{n\mathbf{k}-\mathbf{q}} - \epsilon_{m\mathbf{k}} + \hbar\omega + i\delta} \times \langle n\mathbf{k} - \mathbf{q}|e^{-i(\mathbf{q}+\mathbf{G})\cdot\mathbf{r}}|m\mathbf{k}\rangle \langle m\mathbf{k}|e^{i(\mathbf{q}+\mathbf{G}')\cdot\mathbf{r}}|n\mathbf{k} - \mathbf{q}\rangle$$
(4)

where $(\mathbf{G}, \mathbf{G}')$ is a couple of reciprocal lattice vectors, $\epsilon_{m\mathbf{k}}$ are the Kohn-Sham energies for band m and wave vector \mathbf{k} , $f_{m,\mathbf{k}} \equiv f(\epsilon_{m\mathbf{k}})$ are the occupation numbers within the Fermi-Dirac distribution f at temperature T, v is the unit cell volume and N is the number of kpoints included in the summation. In this expression, the time dependence of the field was assumed to be $e^{-i\omega t}$ and the small positively defined constant δ guarantees that the matrix elements of $\epsilon(\omega)$ are analytic functions in the upper half plane. The macroscopic dielectric

tensor $\overline{\overline{\epsilon}}(\omega)$ is a 3×3 matrix given by:

$$\hat{\mathbf{q}}^{\top} \ \overline{\epsilon}(\omega) \ \hat{\mathbf{q}} = 1 / \lim_{\mathbf{q} \to 0} \epsilon_{\mathbf{0},\mathbf{0}}^{-1} = \lim_{\mathbf{q} \to 0} \epsilon_{0,0}(\mathbf{q},\omega) - \lim_{\mathbf{q} \to 0} \sum_{\mathbf{G},\mathbf{G}' \neq \mathbf{0}} \epsilon_{0,\mathbf{G}}(\mathbf{q},\omega) \epsilon_{\mathbf{G},\mathbf{G}'}^{-1}(\mathbf{q},\omega) \epsilon_{\mathbf{G}',0}(\mathbf{q},\omega), \quad (5)$$

where $\hat{\mathbf{q}}$ is a unitary vector along the wavevector \mathbf{q} . Neglecting the local field (LF) effects amounts to assuming that the dielectric matrix is diagonal, i.e. to neglecting the second term in Eq. 5. Given the hexagonal symmetry of Bi₂Te₃, $\overline{\epsilon}(\omega)$ is diagonal with only two independent elements, namely $\epsilon_{\perp}(\omega)$ and $\epsilon_{\parallel}(\omega)$ that are respectively obtained for $\hat{\mathbf{q}}$ perpendicular and $\hat{\mathbf{q}}$ parallel to the trigonal axis. The dielectric matrix defined in Eq. 4 is computed with the YAMBO code^{35,36} which requires the ground state electronic structure computed with the ABINIT code^{24,25}. Indeed, the Kohn-Sham eigenvalues $\epsilon_{m\mathbf{k}}$ and eigenvectors $|m\mathbf{k}\rangle$ are key ingredients to compute the dielectric function at the RPA level. From a practical point of view, we used a $64 \times 64 \times 64$ kpoints grid (22913 irreducible kpoints) and included 28 valence bands and 34 conduction bands in our calculations to converge the dielectric function without LF effects. The LF effects are included by taking into account the second term in Eq. 5, where a 302×302 body matrix $\epsilon_{\mathbf{G},\mathbf{G}'}(\mathbf{q} \to \mathbf{0},\omega)$ with $\mathbf{G},\mathbf{G}' \neq \mathbf{0}$, ensures the convergence of the macroscopic dielectric function.

Both the imaginary part and the real part of the dielectric function $\epsilon_{\perp,\parallel}(\omega)$ computed with LF effects (thick black lines) and without LF effects (blue dashed lines) at T=300K are displayed in Fig. 4 and compared to the experimental results 19,20 shown as circles and diamonds in the upper pannels of Fig. 4. The imaginary part of the dielectric function computed without LF effects for an electric field $\mathbf{E} \perp \mathbf{c}$ (see Fig. 4(a)) displays two peaks respectively located at 0.32 eV and 1.21 eV while the experimental peaks²⁰ are respectively located at 0.42 eV and 1.22 eV. Such a difference might be related to our crude implementation of the self-energy corrections (the conduction bands have been shifted from 120 meV with respect to the valence bands) or to excitonic effects neglected at our level of approximation^{23,37,38}. It's important to point out that the peak located at 0.32 eV is sensitive to the temperature T and disappears at T = 300 K when the conduction bands are not shifted, which can be explained by the unphysical thermal excitation of electrons from the highest valence band to the lowest conduction band arising from the tiny indirect band gap ~ 42 meV at the LDA level. We also observe that the LF effects do not affect the positions of the peaks but slightly reduce the intensity of the peak located at 1.21 eV. The situation is clearly different for $\mathbf{E} \parallel \mathbf{c}$ (see Fig. 4(c)). Indeed, the imaginary part of the

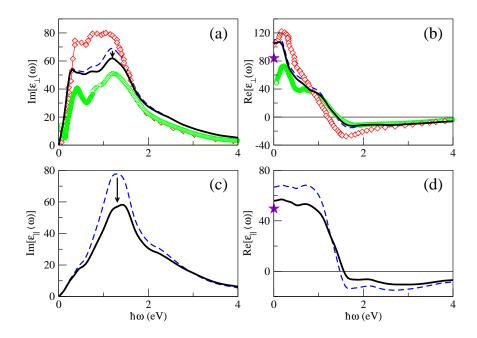


FIG. 4. Imaginary and real part of the dielectric function of Bi_2Te_3 computed at the RPA level with LF effects (thick black lines) and without LF effects (blue dashed lines) for an electric field perpendicular to the trigonal axis (upper pannels) and parallel to the trigonal axis (lower pannels) as a function of the photon energy $\hbar\omega$ (in eV). All the conduction bands have been shifted from 120 meV with respect to the valence bands in order to roughly reproduce the self-energy corrections. The imaginary and real part of the dielectric function obtained from ellipsometry measurements²⁰ and from a Kramers Kronig analysis of reflectivity measurements¹⁹ are respectively displayed as green circles and red diamonds in the upper pannels. The two vertical arrows in pannels (a) and (c) show how the imaginary part of the dielectric function evolves when LF effects are included. The stars in pannel (b) and (d) denote the experimental clamped-nuclei static dielectric constants extracted from the IR reflectance spectras measured at 300 K¹⁷.

dielectric function computed without LF effects displays one peak located at 1.31 eV which is shifted to 1.43 eV when LF effects are included. Furthermore, the intensity of this peak is decreased by ~ 25 % when LF effects are included, suggesting that LF effects are crucial to predict the optical properties for $\mathbf{E} \parallel \mathbf{c}$. This observation is somehow expected as the LF effects, vanishing for an homogeneous electron gas, are as large as the degree of inhomogeneity in the charge density is

undeniably strong along the trigonal axis, namely the stacking axis of the quintuple layers.

We observe a discrepancy between theory and experiment as our calculated imaginary part of the dielectric function for $\mathbf{E} \perp \mathbf{c}$ (see Fig. 4(a)) falls in between the two experimental results^{19,20}. Importantly, the two experimental results only coincide above 3 eV, where the anisotropy in the optical response starts to be negligible as shown in our calculations with or without LF effects. The experimental results of Ref. ¹⁹ are deduced from a Kramers-Kronig (KK) transformation of the near-normal incidence reflectivity spectra for $\mathbf{E} \perp \mathbf{c}$. Thus, both the real and imaginary part of the dielectric function might be erroneous because they are very sensitive to small errors in the reflectivity data and in the high energy extrapolation. The experimental results obtained from ellipsometry measurements²⁰ might also be in error as the authors assumed that they only probe the in-plane component of the dielectric function (ϵ_{\perp}) in the oblique geometry of their measurements while they also probed the out of plane component of the dielectric function (ϵ_{\parallel}) , introducing some errors in the determination of ϵ_{\perp} as our calculations show that the anisotropy in the optical response up to 3 eV is far from being negligible. Therefore, it's difficult to draw a definitive conclusion as two measurements do not lead to the same results, highlighting the need for new experimental studies. It's also important to point out that excitonic effects, neglected at the RPA level, might change the calculated dielectric function. However, excitonic effects are expected to be small because of the large dielectric screening. Indeed, our clamped-nuclei static dielectric constants $\epsilon_{\infty,\perp}$ and $\epsilon_{\infty,\parallel}$ with (without) LF effects are respectively equal to 105 (110) and 56 (67), while the experimental static dielectric constants infered from infrared spectroscopy measurements 17 and shown as stars in Fig. 4(b) and 4(d), are respectively equal to 85 and 50. Such a large contribution of the electrons to the static dielectric constants can be understood from the Kramers Kronig transformation that relates the real part of the dielectric function to the imaginary part of the dielectric function. Indeed, we have

$$\epsilon_{\infty,\perp,\parallel} = \frac{2}{\pi} \int_0^\infty d\omega \, \frac{\operatorname{Im}\left[\epsilon_{\perp,\parallel}(\omega)\right]}{\omega}.\tag{6}$$

As $\operatorname{Im}\left[\epsilon_{\perp}(\omega)\right] > \operatorname{Im}\left[\epsilon_{\parallel}(\omega)\right]$ for $\hbar\omega$ below 1.4 eV , we can conclude that $\epsilon_{\infty,\perp} > \epsilon_{\infty,\parallel}$ since the anisotropy in the optical response is weak above 1.4 eV when LF effects are included. Furthermore, $\epsilon_{\infty,\perp}$ and $\epsilon_{\infty,\parallel}$ are very large because of strong interband transitions starting from 210 meV (direct LDA band gap increased from 120 meV) that strongly contribute to the static dielectric constant because of the $1/\omega$ weighting factor in the integrand of Eq. 6.

Interestingly, as shown in Fig. 4(b) and Fig. 4(d), the real part of ϵ_{\perp} (ϵ_{\parallel}) including LF effects crosses the zero axis around 1.42 eV (1.56 eV) and becomes negative up to 6 eV. Thus, plasmonic applications, as nicely demonstrated in Ref.²¹, can be envisionned but with the inconvenient that the imaginary part of the dielectric function is far from being negligible in this spectral range, especially in the visible range. Our calculations also show that Bi₂Te₃ behaves as an hyperbolic material in a very narrow range of energy between 1.42 and 1.56 eV where the permittivity components in different directions have opposite sign ($\epsilon_{\perp} \cdot \epsilon_{\parallel} < 0$). Therefore, our theoretical results contradict the ellipsometry measurements of Ref.²², where the authors claimed that Bi₂Te₃ is a natural hyperbolic material in the visible range. Such a discrepancy might be ascribed to the fact that the real part of the dielectric function for $\mathbf{E} \parallel \mathbf{c}$ is incorrectly measured.

We also computed the normal incidence reflectivity according to

$$R_{\perp,\parallel}(\omega) = \left| \frac{n_{\perp,\parallel}(\omega) - 1}{n_{\perp,\parallel}(\omega) + 1} \right|^2,\tag{7}$$

where $n_{\perp,\parallel}(\omega) = \sqrt{\epsilon_{\perp,\parallel}(\omega)}$ is the optical index calculated with or without LF effects for $\mathbf{E} \perp \mathbf{c}$ or $\mathbf{E} \parallel \mathbf{c}$. As shown in Fig. 5(a), the overall agreement between theory and experiment¹⁹ for $\mathbf{E} \perp \mathbf{c}$ is fairly good when LF effects are included. It's worth remarking that LF effects do not change the reflectivity spectra very much between 0 eV and 4 eV as can be inferred from Fig. 4(a) and Fig. 4(b) but lead to a strong decrease of the calculated reflectivity from 6 to 9 eV bringing the calculated spectra in closer agreement with the experimental spectra¹⁹. The situation is more contrasted for $\mathbf{E} \parallel \mathbf{c}$ as LF effects are noticeable everywhere. As shown in Fig. 5(b), the calculated reflectivity with LF effects is much smaller than the calculated reflectivity without LF effects almost everywhere up to 9 eV, except for a narrow range of energy between 5.5 eV and 6.4 eV, where the reflectivity displays a dip.

VI. FREQUENCIES AT THE ZONE CENTER

As the primitive cell contains five atoms, there are 15 lattice dynamical modes at the Brillouin zone center, three of which are acoustic modes. Group theory classifies the remaining 12 optical modes into 2 A_{1g} (R), 2 E_g (R), 2 A_{2u} (IR) and 2 E_u (IR) modes, where R and IR refer to Raman and infrared active modes respectively. We computed the zone center frequencies within a DFPT approach³⁹ for the experimental structure at 300 K^{27} ,

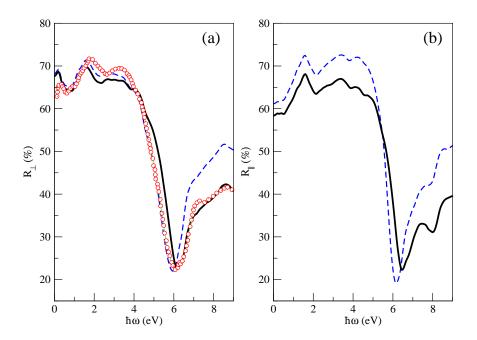


FIG. 5. Computed optical reflectivity with (thick black lines) and without (thin blue dashed lines) LF effects for $\mathbf{E} \perp \mathbf{c}$ (left pannel) and $\mathbf{E} \parallel \mathbf{c}$ (right pannel) compared to the near-normal incidence reflectance spectra (open circles) measured at 300 K for $\mathbf{E} \perp \mathbf{c}^{19}$.

where only the internal coordinates have been relaxed (see table I). As shown in Table II, the overall agreement between theory and experiment^{17,40} is satisfactorily and the largest discrepancy occurs for the A_{1g}^1 and E_u^1 frequencies that are respectively underestimated and overestimated from 8% with respect to the experimental frequencies. Such a difference might be ascribed to anharmonic effects not captured in our calculations⁴¹.

VII. BORN EFFECTIVE CHARGES

We used a finite electric field approach⁴² in order to compute the Born effective charge tensors. The force along β acting on atom p reads

$$F_p^{\beta} = e \sum_{\alpha} Z_{p,\alpha,\beta}^* E^{\alpha}, \tag{8}$$

where E^{α} is the component along α of the macroscopic electric field and $Z_{p,\alpha,\beta}^*$ is the Born effective charge tensor defined for each atom p. Given the hexagonal symmetry of Bi₂Te₃,

TABLE II. Experimental and theoretical values of Raman and infrared phonon frequencies for Bi₂Te₃ in units of cm⁻¹. Experimental Raman^{17,40} and infrared values¹⁷ were measured at 300 K. The values within parentheses correspond to the frequencies in THz and the most recent experimental results⁴⁰ are underlined.

| Symmetry | Experimen | Theory | | |
|-----------------------|---------------------------------|------------|---------------|--|
| E_g^1 | - | 37 (1.11) | 36.81 (1.10) | |
| ${\mathcal A}^1_{1g}$ | 62.5 (1.87) | 62 (1.86) | 57.25 (1.71) | |
| E_g^2 | 103 (3.09) | 102 (3.06) | 97.96 (2.93) | |
| ${\mathcal A}^2_{1g}$ | $134 \ (4.02)$ | 135 (4.05) | 129.25 (3.87) | |
| \mathbf{E}^1_u | $50 \pm 2 \ (1.50 \ \pm 0.06)$ | | 54.25 (1.62) | |
| \mathbf{A}^1_{2u} | $94 \pm 4 \ (2.82 \ \pm 0.12)$ | | 93.23 (2.79) | |
| \mathbf{E}^2_u | $95 \pm 5 \ (2.85 \ \pm 0.15)$ | | 91.75 (2.75) | |
| A_{2u}^2 | $120 \pm 5 \ (3.60 \ \pm 0.15)$ | | 120.25 (3.60) | |

the tensor is diagonal and reduces to two values $Z_{p,\perp}^* = Z_{p,1,1}^* = Z_{p,2,2}^*$ and $Z_{p,\parallel}^* = Z_{p,3,3}^*$ for each atom. Using Eq. 8, we conclude that

$$\begin{cases} F_p^{\beta} = Z_{p,\perp}^* E^{\beta} & \text{when } \beta = 1, 2 \\ F_p^{\beta} = Z_{p,\parallel}^* E^{\beta} & \text{when } \beta = 3 \end{cases}$$
 (9)

Thus, we computed the forces acting on each atom for an electric field perpendicular and parallel to the trigonal axis whose amplitude is varied from -10^{-6} a.u to 10^{-6} with a step of 0.5×10^{-6} a.u (2.57 kV.cm^{-1}). As shown in Fig. 6, the forces F_p acting on each atom p vary linearly with the amplitude of the macroscopic electric field E. A linear fitting provides the Born effective charges that are gathered in table III. It's worth pointing out that the acoustic sum rule $\sum_p Z_{p,\perp}^*$ or \parallel is fulfilled to within 10^{-5} suggesting that our calculations are well converged. The effective charges are large and differ strongly from what can be expected for fully ionic configurations corresponding to closed shell ions (+3 for Bi and -2 for Te). However, it's worth reminding that effective charges are dynamic only and reflect the effect of covalency⁴³. Interestingly, the Born effective charges have surprisingly different values for the Te₁ and Te₂ atoms and show large anisotropy for the Te₁ atoms that form strongly covalent bonds with the Bi atoms as the distance between the Te₁ and Bi atoms is the shortest one. The Born effective charges of Bi atoms also display some degree of

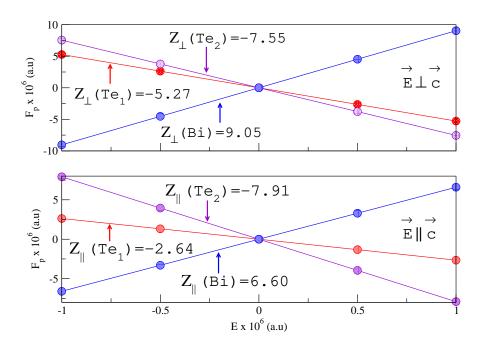


FIG. 6. Forces F_p (in a.u) as a function of the macroscopic electric field E (in a.u) applied perpendicular (upper pannel) and parallel (lower pannel) to the trigonal axis for the experimental structure at 300 K²⁷.

TABLE III. Calculated Born effective charges for the two equivalent Bi atoms, the two equivalent Te_1 atoms and the Te_2 atom underlying the five-point basis. The degree of anisotropy in the Born effective charges is quantified by $Z_{\parallel}^*/Z_{\perp}^*$.

| | Bi | Te_1 | Te_2 |
|------------------------------|-------|-----------------|-----------------|
| $\mathrm{Z}_{\parallel}^{*}$ | 6.60 | -2.64 | -7.91 |
| Z_{\perp}^{*} | 9.05 | -5.27 | -7.55 |
| Z_\parallel^*/Z_\perp^* | 0.729 | 0.500 | 1.047 |

anisotropy. From a physical point of view, the two Bi atoms and the two Te₁ atoms behave respectively as anisotropic cations and anions, while the Te₂ atom behaves as an isotropic anion.

VIII. INFRARED DIELECTRIC TENSOR

We consider a unit cell of volume v containing n atoms. The total energy of the unit cell E_{tot} , when a macroscopic electric field \mathbf{E} is applied, can be taylor expanded as:

$$E_{tot} = E_0 + \frac{1}{2} \sum_{p,p',\alpha,\alpha'} u_p^{\alpha} \frac{\partial^2 E_{tot}}{\partial u_p^{\alpha} \partial u_{p'}^{\alpha'}} u_{p'}^{\alpha'} + \sum_{p,\alpha,\beta} \frac{\partial^2 E_{tot}}{\partial u_p^{\alpha} \partial E^{\beta}} u_p^{\alpha} E^{\beta} + \frac{1}{2} \sum_{\alpha,\beta} \frac{\partial^2 E_{tot}}{\partial E^{\alpha} \partial E^{\beta}} E^{\alpha} E^{\beta}, \quad (10)$$

where u_p^{α} is the displacement of atom p ($p \in \{1, \dots, n\}$) along the direction α and E^{β} the component of the macroscopic field along β with $\alpha, \beta \in \{1, 2, 3\}$. We can introduce the elastic constants $C_{p,p'}^{\alpha,\alpha'}$, the dimensionless Born effective charge tensor $Z_{p,\beta,\alpha}^*$ and the dimensionless electronic tensor susceptibility $\chi_{\alpha,\beta}$, respectively defined by

$$C_{p,p'}^{\alpha,\alpha'} = \frac{\partial^2 E_{tot}}{\partial u_p^{\alpha} \partial u_{p'}^{\alpha'}}, \ Z_{p,\beta,\alpha}^* = -\frac{1}{e} \frac{\partial^2 E_{tot}}{\partial u_p^{\alpha} \partial E^{\beta}}, \ \text{and} \ \chi_{\alpha,\beta} = -\frac{1}{v\epsilon_0} \frac{\partial^2 E_{tot}}{\partial E^{\alpha} \partial E^{\beta}}.$$
 (11)

Thus, the total energy reads

$$E_{tot} = E_0 + \frac{1}{2} \sum_{p,p',\alpha,\alpha'} u_p^{\alpha} C_{p,p'}^{\alpha,\alpha'} u_{p'}^{\alpha'} - e \sum_{p,\alpha,\beta} Z_{p,\beta,\alpha}^* u_p^{\alpha} E^{\beta} - \frac{1}{2} v \epsilon_0 \sum_{\alpha,\beta} \chi_{\alpha,\beta} E^{\alpha} E^{\beta}, \qquad (12)$$

leading to a force (See Eq. 8) exerted on atom p by the macroscopic electric field when the atoms are held at their equilibrium position. From Eq. 12, we get the component along β of the polarization

$$P^{\beta} = -\frac{1}{v} \frac{\partial E_{tot}}{\partial E^{\beta}} = P^{\beta,ion} + P^{\beta,el}, \tag{13}$$

where the ionic contribution to the polarization reads

$$P^{\beta,ion} = \frac{e}{v} \sum_{\alpha,p} Z_{p,\beta,\alpha}^* u_p^{\alpha}, \tag{14}$$

and the electronic contribution reads

$$P^{\beta,el} = \epsilon_0 \sum_{\alpha} \chi_{\beta,\alpha} E^{\alpha}. \tag{15}$$

Using Eq. 12, the equation of motion for atom p of mass M_p reads

$$M_p \ddot{u}_p^{\alpha} = -\frac{\partial E_{tot}}{\partial u_p^{\alpha}} = -\sum_{p',\alpha'} C_{p,p'}^{\alpha,\alpha'} u_{p'}^{\alpha'} + e \sum_{\beta} Z_{p,\beta,\alpha}^* E^{\beta}.$$
 (16)

When $\mathbf{E} = \mathbf{0}$, we can plug

$$u_p^{\alpha} = \sqrt{\frac{M}{M_p}} \epsilon_p^{\alpha} \exp[-i\omega t], \tag{17}$$

where $M = \sum_{p} M_{p}$, in Eq. 16 and solve the following eigenvalue problem

$$\sum_{p',\alpha'} D_{p,p'}^{\alpha,\alpha'} \epsilon_{p'}^{\alpha'}(\lambda) = \omega_{\lambda}^2 \epsilon_p^{\alpha}(\lambda), \tag{18}$$

where $D_{p,p'}^{\alpha,\alpha'}=C_{p,p'}^{\alpha,\alpha'}/\sqrt{M_pM_{p'}}$ is the dynamical matrix at the zone center. Here ω_{λ} and $\epsilon_p^{\alpha}(\lambda)$ are respectively the frequency and the displacement of atom p along α for the mode λ , where $\lambda \in \{1, \dots, 3n\}$. The eigenvectors of Eq. 18 satisfy the orthogonality relations

$$\sum_{p,\alpha} \epsilon_p^{\alpha}(\lambda) \epsilon_p^{\alpha}(\lambda') = \delta_{\lambda,\lambda'} \Longleftrightarrow \epsilon(\lambda)^{\top} \epsilon(\lambda') = \delta_{\lambda,\lambda'}, \tag{19}$$

since the zone center dynamical matrix is real and symmetric.

When $\mathbf{E} = \mathbf{E}_0 \exp(-i\omega t)$, where ω is the frequency of the electric field in the THz range, we can plug

$$u_p^{\alpha} = \sqrt{\frac{M}{M_p}} z_p^{\alpha} \exp[-i\omega t], \qquad (20)$$

into Eq. 16. Thereby, the following equation

$$\omega^2 z_p^{\alpha} = \sum_{p',\alpha'} D_{p,p'}^{\alpha,\alpha'} z_{p'}^{\alpha'} - \frac{e}{\sqrt{MM_p}} \sum_{\beta} Z_{p,\beta,\alpha}^* E_0^{\beta}$$
(21)

must be solved. As $\{\epsilon(\lambda), \lambda = 1, \dots, 3n\}$ forms a complete basis set, we can seek a solution in the form

$$z_p^{\alpha} = \sum_{\lambda} A(\lambda) \epsilon_p^{\alpha}(\lambda), \tag{22}$$

where the coefficients $A(\lambda)$ have to be determined. Introducing Eq. 22 in Eq. 21 and using Eq. 18 leads to

$$\sum_{\lambda'} A(\lambda') \left[\omega^2 - \omega_{\lambda'}^2 \right] \epsilon_p^{\alpha}(\lambda') = -\frac{e}{\sqrt{MM_p}} \sum_{\beta} Z_{p,\beta,\alpha}^* E_0^{\beta}$$
 (23)

By multiplying this identity with $\epsilon_p^{\alpha}(\lambda)$, summing over p and α and using the orthogonality relation (Eq. 19), we obtain

$$A(\lambda) = -\frac{e}{M} \frac{1}{\omega^2 - \omega_\lambda^2} \sum_{\beta'} Z_{\beta'}(\lambda) E_0^{\beta'}, \tag{24}$$

where the mode effective charge

$$Z_{\beta}(\lambda) = \sum_{p,\alpha} \sqrt{\frac{M}{M_p}} \epsilon_p^{\alpha}(\lambda) Z_{p,\beta,\alpha}^*, \tag{25}$$

is a dimensionless quantity. Plugging Eq. 24 in Eq. 22, and using the definition of ionic polarization (Eq. 14) as well as Eq. 20, we obtain

$$P^{\beta,ion}(\omega) = \frac{e^2}{v} \frac{1}{M} \sum_{\beta',\lambda} \frac{Z_{\beta}(\lambda) Z_{\beta'}(\lambda)}{\omega_{\lambda}^2 - \omega^2} E^{\beta'}$$
 (26)

By analogy with the definition of the electronic susceptibility (Eq. 15), we can define an ionic susceptibility

$$\chi_{\beta,\beta'}^{ion}(\omega) = \frac{e^2}{\epsilon_0 v} \frac{1}{M} \sum_{\lambda} \frac{S_{\beta,\beta'}(\lambda)}{\omega_{\lambda}^2 - \omega^2 - 2i\omega\gamma_{\lambda}},\tag{27}$$

where $2\gamma_{\lambda}$ is the full width at half maximum (FWHM) of the phonon peak and $S_{\beta,\beta'}(\lambda) = Z_{\beta}(\lambda)Z_{\beta'}(\lambda)$ is a dimensionless 3×3 real symmetric matrix. It's straightforward to show using Eq. 25 that this matrix S is zero for a gerade mode. Interestingly, S might be non diagonal for degenerated modes like the E_u^1 mode at 1.62 THz or the E_u^2 mode at 2.75 THz that can couple to an electric field perpendicular to the trigonal axis. However, the matrix S becomes diagonal when the polarization of the first E_u mode is chosen along one of the two fold axis (x-axis) while the polarization of the second E_u mode lies along one of the mirror plane (y-axis). Thus, we get:

$$\chi_{\perp,\parallel}^{ion}(\nu) = \frac{e^2}{4\pi^2 \epsilon_0 v} \frac{1}{M} \sum_{\lambda} \frac{S_{\perp,\parallel}(\lambda)}{\nu_{\lambda}^2 - \nu^2 - i\nu\gamma_{\lambda}/\pi},\tag{28}$$

where $S_{\perp}(\lambda) = [Z_1(\lambda)]^2$ or $[Z_2(\lambda)]^2$, $S_{\parallel}(\lambda) = [Z_3(\lambda)]^2$ (see Eq. 25) and where the summation can be restricted to the IR active modes.

TABLE IV. Frequencies (in THz), oscillator strengths (dimensionless quantities) and normalized atomic displacements (see Eq. 19) for the IR active modes. The calculations have been done for the experimental lattice structure²⁷ using the values of the Born effective charges reported in table III.

Symmetry Frequency Oscillator strengths Normalized atomic displacements Direction

| | | S_{\perp} | S_{\parallel} | Te_1 | Bi | Te_2 | Bi | Te_1 | |
|---------------------|------|-------------|-----------------|--------|--------|--------|--------|-----------------|------|
| E^1_u | 1.62 | 1318.15 | - | 0.310 | -0.475 | 0.596 | -0.475 | 0.310 | x, y |
| \mathbf{E}^2_u | 2.75 | 15.48 | - | 0.494 | -0.114 | -0.696 | -0.114 | 0.494 | x, y |
| \mathbf{A}^1_{2u} | 2.79 | - | 540.46 | 0.122 | 0.262 | -0.913 | 0.262 | 0.122 | z |
| A_{2u}^2 | 3.60 | - | 273.73 | 0.571 | -0.413 | -0.085 | -0.413 | 0.571 | z |

The oscillator strengths S_{\perp} and S_{\parallel} for an electric field respectively perpendicular and parallel to the trigonal axis are reported in table IV. We have previously seen that the

oscillator strengths are related to both the eigenvectors of the zone center dynamical matrix and the mode effective charges (See Eq. 25). The huge difference between the oscillator strength for the E_u^1 and E_u^2 modes arises from the fact that all atoms contribute to S_{\perp} for the E_u^1 mode while only the Bi atoms contribute significantly for the E_u^2 mode. Indeed, the displacements of atoms have the same sign for both modes with the exception of the Te₂ atom whose displacement along the E_u^2 mode is reversed, producing an almost complete cancellation of the Te atoms to S_{\perp} . For the sake of completeness, the displacements of atoms

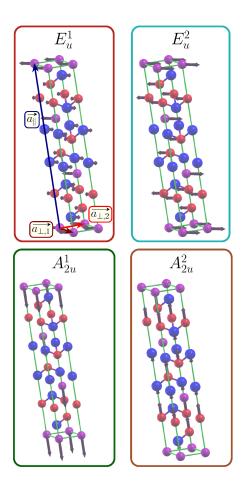


FIG. 7. Displacements of the atoms for the two E_u modes polarized along the x-axis and for the two A_{2u} modes polarized along the z-axis (trigonal axis). The Te₁, Te₂ and Bi atoms are respectively colored in red, purple and blue.

inside the hexagonal unit cell for the four different IR active modes are depicted in Fig. 7.

The IR dielectric constant is defined as

$$\epsilon_{\perp,\parallel}(\nu) = \epsilon_{\infty,\perp,\parallel} + \chi_{\perp,\parallel}^{ion}(\nu), \tag{29}$$

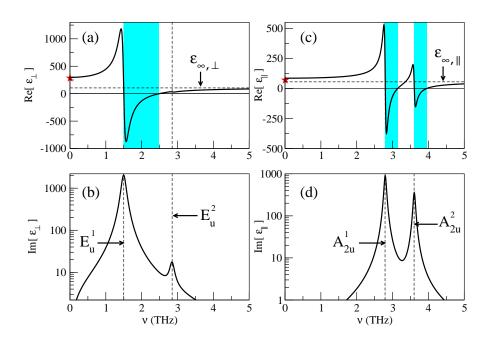


FIG. 8. Imaginary and real part of the IR dielectric function of Bi_2Te_3 computed with Eq. 28 for an electric field perpendicular to the trigonal axis (pannels a and b) and parallel to the trigonal axis (pannels c and d) as a function of frequency ν (in THz). We assumed that $\gamma_{\lambda} = 0.44$ THz for the E_u modes and that $\gamma_{\lambda} = 0.22$ THz for the A_{2u} modes. Note that the frequencies of both E_u modes have been slightly renormalized to match the experimental frequencies¹⁷ reported in table II while the theoretical frequencies of both A_{2u} modes have been considered. The stars in pannel (a) and (c) denote the experimental static dielectric constants extracted from the IR reflectance spectras measured at 15 K¹⁷ and the colored domain in pannel (a) delimits the Restrahlen band of the E_u^1 mode situated between the transversal optical frequency at 1.5 THz and the longitudinal optical frequency at 2.49 THz while the two colored domains in pannel (c) delimit the Restrahlen bands of the A_{2u}^1 (A_{2u}^2) mode situated between the transversal optical frequency at 2.79 THz (3.60 THz) and the longitudinal optical frequency at 3.14 THz (3.95 THz).

where the electronic contribution to the static dielectric function at the RPA level denoted as $\epsilon_{\infty,\perp,\parallel}$, also named clamped-nuclei dielectric constant, can be approximated as a constant for frequencies less than 5 THz. Fig. 8(a) and 8(c) display the real part of the IR dielectric function computed for an electric field perpendicular ($\mathbf{E} \perp \mathbf{c}$) and parallel ($\mathbf{E} \parallel \mathbf{c}$) to the trigonal axis. The two E_u modes can be driven for $\mathbf{E} \perp \mathbf{c}$ while the two A_u modes can

be driven for $\mathbf{E} \parallel \mathbf{c}$. The real part changes sign each time the frequency ν crosses the frequency of an IR active mode depicted as a vertical dashed line in Fig. 8. The only exception concerns the mode E_u^2 whose oscillator strength is very weak (see Table IV). Interestingly, our calculations reproduce the static dielectric functions denoted as stars for both polarizations. The ionic and electronic contributions to the total susceptibility are respectively ~ 192 and ~ 104 (~ 29 and ~ 55) for $\mathbf{E} \perp \mathbf{c}$ ($\mathbf{E} \parallel \mathbf{c}$), reflecting the high degree of anisotropy of the optical properties in the THz range. It's worth outlining that $\mathrm{Re}[\epsilon_{\perp}].\mathrm{Re}[\epsilon_{\parallel}] < 0$ for the three Restrahlen bands depicted as vertical colored domains in Fig. 8. Hence, $\mathrm{Bi}_2\mathrm{Te}_3$ as h-BN⁴⁴ or α -MoO3⁴⁵ exhibits natural hyperbolicity and might support hyperbolic phonon-polaritons. We also note that the imaginary part of the IR dielectric function displayed in Fig. 8(b) and 8(d) has a lorentzian profile in the vicinity of each resonance with a full width at half maximum (FHWM) given by γ_{λ}/π and remind that the phonon lifetime is given by $1/\gamma_{\lambda}$. Here, we assumed that the lifetimes of both E_u modes is ~ 2.27 ps while the lifetimes of both A_u modes is ~ 4.54 ps to best reproduce the IR reflectance spectras discussed in the following section.

IX. INFRARED REFLECTIVITY SPECTRUM

The normal incidence reflectivity spectras computed according to Eq. 7 for $\mathbf{E} \perp \mathbf{c}$ and $\mathbf{E} \parallel \mathbf{c}$ are compared to the experimental spectras at 15 K¹⁷ in Fig. 9. Roughly speaking, the overall agreement between the calculated reflectivity (dashed lines) and the experimental reflectivity (open circles) for both polarizations is fairly good within the Restrahlen bands, while poor outside, suggesting that the free electrons arising from doping contribute to the dielectric function. Hence, we consider the dielectric function

$$\overline{\epsilon}_{\perp,\parallel}(\nu) = \epsilon_{\perp,\parallel}(\nu) - \nu_{pl,\perp,\parallel}^2 / \nu(\nu + i\gamma_{\perp,\parallel}), \tag{30}$$

where $\epsilon_{\perp,\parallel}$ is defined in Eq. 29 and where the charge carrier contribution depends on two parameters, namely the plasmon frequency $\nu_{pl,\perp,\parallel}$ and plasmon damping $\gamma_{\perp,\parallel}$. The calculated reflectivity shown as a solid line in Fig. 9 for $\mathbf{E} \perp \mathbf{c}$ ($\mathbf{E} \parallel \mathbf{c}$) with $\nu_{pl,\perp} \sim 26.6$ THz ($\nu_{pl,\parallel} \sim 24.2$ THz) reproduces nicely the experimental reflectivity provided that the plasmon damping constant γ_{\perp} (γ_{\parallel}) is well chosen. We found that a constant plasmon damping $\gamma_{\perp} \sim 0.95$ THz allows to reproduce the experimental reflectivity spectra for $\mathbf{E} \perp \mathbf{c}$ while a

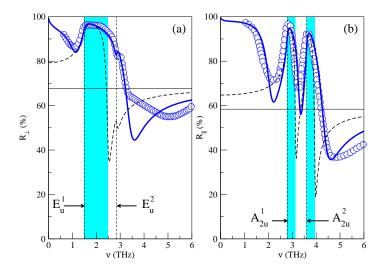


FIG. 9. Computed IR reflectivity spectras with (thick lines) and without (dashed lines) the free electron contribution for $\mathbf{E} \perp \mathbf{c}$ (left pannel) and $\mathbf{E} \parallel \mathbf{c}$ (right pannel) compared to the experimental spectras (open circles) recorded at 15 K¹⁷. The restrahlen bands are depicted as colored domains and the horizontal lines correspond to the expected value of the reflectivity well above the highest IR frequency (~ 3.6 THz) but below the band gap frequency (~ 51 THz).

frequency dependent plasmon damping γ_{\parallel} is crucial to reproduce the reflectivity spectra for $\mathbf{E} \parallel \mathbf{c}$. Hence, we considered the following formula:

$$\gamma_{\parallel}(\nu) = \frac{\gamma_l + \gamma_h}{2} + \frac{\gamma_h - \gamma_l}{2} \tanh\left(\frac{\nu - \nu_0}{\Delta \nu}\right), \tag{31}$$

to interpolate between the low frequency value of the plasmon damping denoted as $\gamma_l \sim 0.24$ THz and the high frequency value, denoted as $\gamma_h \sim 1.7$ THz with a fairly steep variation in a frequency interval $2\Delta\nu \sim 1.4$ THz centered on $\nu_0 \sim 2.3$ THz.

X. PLASMON FREQUENCIES

As shown in the previous part, the Drude contribution to the IR reflectivity can not be ignored. Indeed, a bulk charge carrier contribution originates from intrinsic defects, such as anion vacancies and antisite defects that are ubiquitous in most compound semiconductors⁴⁶. For instance, focusing on the latter, either a Te₁ atom can be replaced by a Bi atom, leading to hole charge carriers or a Bi atom can be replaced by a Te atom, leading to

electron charge carriers. From an experimental point of view, the p-type or n-type charge carrier concentration can range from 3×10^{17} to 5×10^{19} cm⁻³, depending on the growth conditions. Assuming that the rigid band model is valid, the plasma frequencies can be

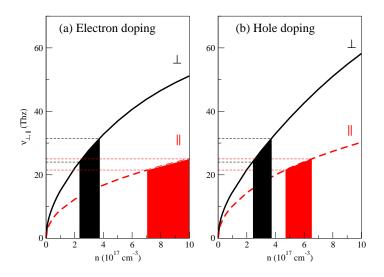


FIG. 10. Plasmon frequencies $\nu_{pl,\perp}$ and $\nu_{pl,\parallel}$ (in THz) computed as a function of electron doping (left pannel) and hole doping (right pannel) up to $n=10^{18}$ cm⁻³. The horizontal dashed lines of the same color span the range of plasmon frequencies that gives a good fitting of the reflectivity spectras shown in Fig. 9. The range of doping corresponding to the range of $\nu_{pl,\perp}$ ($\nu_{pl,\parallel}$) is depicted in black (red). The plasmon frequencies, that are hard to converge, are computed using a very dense $256 \times 256 \times 256$ grid of kpoints for a temperature $T \sim 15$ K.

evaluated by tuning the Fermi level to achieve either electron or hole doping. In such a case, it is straightforward to show that the intraband contribution to the dielectric tensor defined in Eq. 5 behaves as $-\overline{\omega_{pl}^2}/\omega^2$ where:

$$\omega_{pl,\alpha,\beta}^2 = \frac{e^2}{4\pi\epsilon_0} \frac{4\pi}{v} \frac{1}{N} \sum_{\mathbf{k},n} v_{n\mathbf{k}}^{\alpha} v_{n\mathbf{k}}^{\beta} \left(-\frac{\partial f}{\partial \epsilon} \right)_{\epsilon,\mathbf{k}}.$$
 (32)

Here $\mathbf{v}_{n\mathbf{k}} \equiv \nabla_{\mathbf{k}} \epsilon_{n\mathbf{k}}/\hbar$ are the band velocities. It is important to note that only states at the Fermi level contribute to $\omega_{pl,\alpha,\beta}^2$ at T=0 since $-\frac{\partial f}{\partial \epsilon} \to \delta[\epsilon - \epsilon_F]$ when $T \to 0$ and that $\omega_{pl,\alpha,\beta}^2$ is expected to increase when T increases because of the larger number of states contributing to the sum in Eq. 32. Replacing $\epsilon_{n\mathbf{k}}$ by $\hbar^2 k^2/2m$ in Eq. 32 is tantamount to considering a free electron gas and leads to the classical equation $\omega_{pl}^2 = ne^2/m\epsilon_0$ where n

is the electron density number. In such a case, we obtain an isotropic plasma frequency. For Bi_2Te_3 , the situation is clearly different. Indeed, $\overline{\overline{\omega_{pl}^2}}$ is a diagonal tensor with only two independent elements, namely $\omega_{pl,\perp}^2 \equiv \omega_{pl,1,1}^2 = \omega_{pl,2,2}^2$ and $\omega_{pl,\parallel}^2 \equiv \omega_{pl,3,3}^2$. Furthermore, both the last valence and first conduction band near the six extremas discussed in part IV display a non-parabolic dispersion as shown in Shubnikov-de Haas experiments^{6,7}. We computed the plasmon frequencies $\nu_{pl,\perp,\parallel} = \omega_{pl,\perp,\parallel}/2\pi$ as a function of doping n with n up to 10^{18} cm⁻³, corresponding to a low level of doping ($\sim 1.69 \times 10^{-4}$ electrons or holes per unit cell). As shown in Fig. 10, $\nu_{pl,\perp}$ is larger than $\nu_{pl,\parallel}$ for each n and they both increase when n increases. However, $\nu_{pl,\parallel}$ increases faster for hole doping (See Fig. 10(b)) than for electron doping (See Fig. 10(a)) while $\nu_{pl,\perp}$ does not depend on the type of doping up to $n_c = 4 \times 10^{17} \ {\rm cm}^{-3}$ and becomes larger for hole doping, as compared to electron doping, above n_c . Interestingly, we reported in Fig. 10 the range of $\nu_{pl,\perp}$ (see the dashed black lines) and $\nu_{pl,\parallel}$ (see the dashed red lines) respectively giving a fairly good agreement between theory and experiment for R_{\perp} and R_{\parallel} . The corresponding values of n are colored in black (red) for $\nu_{pl,\perp}$ ($\nu_{pl,\parallel}$). A nice agreement between our fitted and theoretical values involves an overlap between the two colored domains. Neither the calculations for electron doping nor the calculations for hole doping produce such an overlap. However, the two colored domains in Fig. 10(b) are closest to each other, suggesting that the sample used in the experiments¹⁷ might be hole doped with $n \sim 4 \times 10^{17} \ \mathrm{cm}^{-3}$. While our approach to model doping is very crude, our calculations suggest that a measure of the reflectivity spectras in the THz range for both polarizations might be helpful to infer both type and level of doping. The validity of our approach might be assessed by cross-checking the results with Hall measurements.

XI. CONCLUSION

We studied the optical properties of Bi₂Te₃ in both the visible and IR range. Our firstprinciples calculations reveal that the dielectric functions computed at the RPA level are rather anisotropic (a fact disregarded in ellipsometry measurements²⁰) and strongly impacted by the LF effects when the electric field is polarized along the trigonal axis. The agreement between our calculated near-normal incidence reflectivity spectra for an electric field perpendicular to the trigonal axis and the experimental spectra¹⁹ is fairly good, assessing the validity of our approach to compute the optical spectras by simply shifting the

conduction bands with respect to the valence bands from 120 meV to roughly mimic the self-energy corrections. The clamped nuclei static dielectric constants including LF effects $(\epsilon_{\perp}^{\infty} \sim 105 \text{ and } \epsilon_{\parallel}^{\infty} \sim 56)$ are very large because of strong direct interband transitions starting from the direct band gap ~ 210 meV and extending up to 4 eV, suggesting that excitonic effects can be neglected in the optical calculations. The ionic contributions to the static dielectric constants, that can be computed from both the Born effective charges and the IR phonon frequencies and eigenvectors, are also very large as $\chi_{\perp}^{ion}\sim 192$ and $\chi_{\parallel}^{ion}\sim 29$. The huge value for χ_{\perp}^{ion} reflects the strong coupling between an electric field perpendicular to the trigonal axis and the E_u^1 mode. Furthermore, the calculated reflectivity spectras in the THz range agree fairly well with the experimental spectras¹⁷ provided that the unavoidable contribution of the free carriers arising from defects is taken into account by considering a Drude contribution parametrized by plasmon frequencies and plasmon damping that are fitted to reproduce the experimental spectras. We showed that the plasmon frequencies can be computed within the rigid band approximation as a function of both type and level of doping. Thus, a measurement of the reflectivity in the THz range for both polarizations might offer the opportunity to infer not only the type of doping but also the level of doping. Finally, this work is a first step towards the understanding of the mechanisms governing the generation of the coherent A_{1g} phonon in a THz excited $\mathrm{Bi_2Te_3}$ nanofilm⁴⁷ as a non linear coupling between the E_u^1 mode driven by the THz pulse and the A_{1g} mode might be at the heart of the experimental observations⁴⁸.

ACKNOWLEDGMENTS

This work was performed using HPC resources from GENCI-TGCC, CINES, IDRIS (project AD010905096R1).

 $^{^{1}\,}$ G. Snyder and E. Toberer, Complex thermoelectric materials, Nature Mater 7, 105 (2008).

² H. Zhang, C. Liu, X. Qi, , X. Dai, Z. Fang and S. Zhang, Topological insulators in Bi₂Se₃, Bi₂Te₃ and Sb₂Te₃ with a single Dirac cone on the surface, Nature Phys **5**, 438 (2009).

³ Y. L. Chen, J. G. Analytis, J.-H. Chu, Z. K. Liu, S.-K. Mo, X. L. Qi, H. J. Zhang, D. H. Lu, X. Dai, Z. Fang, S. C. Zhang, I. R. Fisher, Z. Hussain and Z.-X. Shen, Experimental Realization

- of a Three-Dimensional Topological Insulator, Bi₂Te₃, Science **325**, 178 (2009).
- ⁴ D. Hsieh, Y. Xia, D. Qian, L. Wray, J. H. Dil, F. Meier, J. Osterwalder, L. Patthey, J. G. Checkelsky, N. P. Ong, A. V. Fedorov, H. Lin, A. Bansil, D. Grauer, Y. S. Hor, R. J. Cava, M. Z. Hasan, A tunable topological insulator in the spin helical Dirac transport regime, Nature 460, 1101 (2009).
- D. Hsieh, Y. Xia, D. Qian, L. Wray, F. Meier, J. H. Dil, J. Osterwalder, L. Patthey, A. V. Fedorov, H. Lin, A. Bansil, D. Grauer, Y. S. Hor, R. J. Cava, and M. Z. Hasan, Observation of Time-Reversal-Protected Single-Dirac-Cone Topological-Insulator States in Bi₂Te₃ and Sb₂Te₃, Phys. Rev. Lett. **103**, 146401 (2009).
- ⁶ H. Kohler, Non-Parabolicity of the Highest Valence Band of Bi₂Te₃ from Shubnikov-de Haas Effect, Phys. Status Solidi B 74, 591 (1976).
- ⁷ H. Kohler, Non-Parabolic E(k) Relation of the Lowest Conduction Band in Bi₂Te₃, Phys. Status Solidi B 73, 95 (1976).
- ⁸ I. Mohelský, A. Dubroka, J. Wyzula, A. Slobodeniuk, G. Martinez, Y. Krupko, B. A. Piot, O. Caha, J. Humlíček, G. Bauer, G. Springholz and M. Orlita, Landau level spectroscopy in Bi₂Te₃, Phys. Rev. B **102**, 085201 (2020).
- ⁹ M. Hajlaoui, E. Papalazarou, J. Mauchain, G. Lantz, N. Moisan, D. Boschetto, Z. Jiang, I. Miotkowski, Y. P. Chen, A. Taleb-Ibrahimi, L. Perfetti, M. Marsi, Ultrafast Surface Carrier Dynamics in the Topological Insulator Bi₂Te₃, Nano Lett. 12, 3532-3536 (2012).
- M. Weis, K. Balin, B. Wilk, T. Sobol, A. Ciavardini, G. Vaudel, V. Juvé, B. Arnaud, B. Ressel, M. Stupar, K. C. Prince, G. De Ninno, P. Ruello, and J. Szade, Hot-carrier and optical-phonon ultrafast dynamics in the topological insulator Bi₂Te₃ upon iron deposition on its surface, Phys. Rev. B 104, 245110 (2021).
- ¹¹ G. Wang and T. Cagin, Electronic structure of the thermoelectric materials Bi₂Te₃ and Sb₂Te₃ from first-principles calculations, Phys. Rev. B **76**, 075201 (2007).
- ¹² X. Luo, M. B. Sullivan, and S. Y. Quek, First-principles investigations of the atomic, electronic, and thermoelectric properties of equilibrium and strained Bi₂Se₃ and Bi₂Te₃ including van der Waals interactions, Phys. Rev. B 86, 184111 (2012).
- E. Kioupakis, M. L. Tiago, and S. G. Louie, Quasiparticle electronic structure of bismuth telluride in the GW approximation, Phys. Rev. B 82, 245203 (2010).
- ¹⁴ O. V. Yazyev, E. Kioupakis, J. E. Moore, and S. G. Louie, Quasiparticle effects in the bulk and

- surface-state bands of Bi_2Se_3 and Bi_2Te_3 topological insulators, Phys. Rev. B **85**, 161101(R) (2012).
- ¹⁵ I. Aguilera, C. Friedrich, G. Bihlmayer and S. Blügel, GW study of topological insulators Bi₂Se₃, Bi₂Te₃ and Sb₂Te₃: Beyond the perturbative one-shot approach, Phys. Rev. B 88, 045206 (2013).
- ¹⁶ I. A. Nechaev, and E. V. Chulkov, Quasiparticle band gap in the topological insulator Bi₂Te₃, Phys. Rev. B 88, 165135 (2013).
- W. Richter, H. Köhler and C.R. Becker, A Raman and Far-Infrared Investigation of Phonons in the Rhombohedral V₂VI₃ Compounds, phys. stat. sol. (b) 84, 619 (1977).
- ¹⁸ B. C. Chapler, K. W. Post, A. R. Richardella, J. S. Lee, J. Tao, N. Samarth, and D. N. Basov, Infrared electrodynamics and ferromagnetism in the topological semiconductors Bi₂Te₃ and Mn-doped Bi₂Te₃, Phys. Rev. B 89, 235308 (2014).
- ¹⁹ D. L. Greenaway and G. Harbeke, Band structure of bismuth telluride, bismuth selenide and their respective alloys, J. Phys. Chem. Solids 26, 1585 (1965).
- A. Dubroka, O. Caha, M. Hroniček, P. Friš, M. Orlita, V. Holý, H. Steiner, G. Bauer, G. Springholz and J. Humlíček, Interband absorption edge in the topological insulators Bi₂(Te_{1-x}Se_x)₃, Phys. Rev. B **96**, 235202 (2017).
- M. Zhao , M. Bosman , M. Danesh , M. Zeng , P. Song , Y. Darma , A. Rusydi , H. Lin , C.-W. Qiu , K. P. Loh, Visible Surface Plasmon Modes in Single Bi₂Te₃ Nanoplate, Nano Lett. 15 , 8331 (2015).
- M. Esslinger, R. Vogelgesang, N. Talebi, W. Khunsin, P. Gehring, S. De Zuani, B. Gompf, and K. Kern, Tetradymites as Natural Hyperbolic Materials for the Near-Infrared to Visible, ACS Photonics 1, 12, 1285–1289 (2014).
- G. Onida, L. Reining, A. Rubio, Electronic excitations: density-functional versus many-body Green's-function approaches, Reviews of modern physics 74 (2), 601 (2002).
- ²⁴ X. Gonze, B. Amadon, P.-M. Anglade, J.-M. Beuken, F. Bottin, P. Boulanger, F. Bruneval, D. Caliste, R. Caracas, M. Côté et al, ABINIT: First-principles approach to material and nanosystem properties, Comput. Phys. Commun. 180, 2582 (2009).
- ²⁵ X. Gonze, F. Jollet, F. Abreu Araujo, D. Adams, B. Amadon, T. Applencourt, C. Audouze, J.-M. Beuken, J. Bieder, A. Bokhanchuk *et al*, Recent developments in the ABINIT software package, Comput. Phys. Commun. **205**, 106 (2016).

- ²⁶ C. Hartwigsen, S. Goedecker, and J. Hutter, Relativistic separable dual-space Gaussian pseudopotentials from H to Rn, Phys. Rev. B 58, 3641 (1998).
- M. H. Francombe, Structure cell data and expansion coefficients of bismuth tellurium, Br. J. Appl. Phys. 9, 415 (1958).
- ²⁸ J. R. Wiese and L. Muldawer, Lattice constants of Bi₂Te₃-Bi₂Se₃ solid solution alloys, J. Phys. Chem. Solids 15, 13 (1960).
- ²⁹ G. A. Thomas, D. H. Rapkine, R. B. Van Dover, L. F. Mattheiss, W. A. Sunder, L. F. Schneemeyer, and J. V. Waszczak, Large electronic-density increase on cooling a layered metal: Doped Bi₂Te₃, Phys. Rev. B 46, 1553 (1992).
- M. S. Hybertsen and S. G. Louie, Electron correlation in semiconductors and insulators: Band gaps and quasiparticle energies, Phys. Rev. B 34, 5390 (1986).
- ³¹ B. Arnaud and M. Alouani, All-electron projector-augmented-wave GW approximation: Application to the electronic properties of semiconductors, Phys. Rev. B **62**, 4464 (2000).
- ³² S. Lebègue, B. Arnaud, M. Alouani and P.E. Bloechl, Implementation of an all-electron GW approximation based on the projector augmented wave method without plasmon pole approximation: Application to Si, SiC, AlAs, InAs, NaH, and KH, Phys. Rev. B 67, 155208 (2003).
- ³³ S.L. Adler, Quantum Theory of the Dielectric Constant in Real Solids, Phys. Rev. 126, 413 (1962).
- ³⁴ N. Wiser, Dielectric Constant with Local Field Effects Included, Phys. Rev. **129**, 62 (1963).
- A. Marini, C. Hogan, M. Grüning, D. Varsano, Yambo: an ab initio tool for excited state calculations, Comput. Phys. Commun. 180, 1392 (2009)
- D. Sangalli, A. Ferretti, H. Miranda, C. Attaccalite, I. Marri, E. Cannuccia, P. Melo, M. Marsili, F. Paleari, A. Marrazzo, G. Prandini, P. Bonfà, M. O Atambo, F. Affinito, M. Palummo, A. Molina-Sánchez, C. Hogan, M Grüning, D. Varsano and A. Marini, Many-body perturbation theory calculations using the yambo code, Journal of Physics: Condensed Matter 31, 325902 (2019)
- ³⁷ B. Arnaud and M. Alouani, Local-field and excitonic effects in the calculated optical properties of semiconductors from first-principles, Phys. Rev. B 63, 085208 (2001)
- ³⁸ B. Arnaud, S. Lebègue, P. Rabiller, and M. Alouani, Huge excitonic effects in layered hexagonal boron nitride, Phys. Rev. Lett. 96, 026402 (2006)
- ³⁹ X. Gonze, First-principles responses of solids to atomic displacements and homogeneous electric

- fields: Implementation of a conjugate-gradient algorithm, Phys. Rev. B 55, 10337 (1997).
- ⁴⁰ C. Wang, X. Zhu, L. Nilsson, J. Wen, G. Wang, X. Shan, Q. Zhang, S. Zhang, J. Jia, and Q. Xue, In situ Raman spectroscopy of topological insulator Bi₂Te₃ films with varying thickness, Nano Res. 6, 688-692 (2013).
- ⁴¹ X. Yang, T. Feng, J. S. Kang, Y. Hu, J. Li, and X. Ruan, Observation of strong higher-order lattice anharmoniticity in Raman and infrared spectra, Phys. Rev. B **101**, 161202(R) (2020).
- ⁴² I. Souza, J. Iñiguez and D. Vanderbilt, First-principles Approach to Insulators in Finite Electric Fields, Phys. Rev. Lett. 89, 117602 (2002).
- Kwan-Woo Lee and W. E. Pickett, Born effective charges and infrared response of LiBC, Phys. Rev. B 68, 085308 (2003).
- Joshua D. Caldwell, Andrey V. Kretinin, Yiguo Chen, Vincenzo Giannini, Michael M. Fogler, Yan Francescato, Chase T. Ellis, Joseph G. Tischler, Colin R. Woods, Alexander J. Giles, Minghui Hong, Kenji Watanabe, Takashi Taniguchi, Stefan A. Maier and Kostya S. Novoselov, Sub-diffractional volume-confined polaritons in the natural hyperbolic material hexagonal boron nitride, Nat. Commun. 5, 5221 (2014).
- W. Ma, P. Alonso-González, S. Li, A. Y. Nikitin, J. Yuan, J. Martín-Sánchez, J. Taboada-Gutiérrez, I. Amenabar, P. Li, S. Vélez, C. Tollan, Z. Dai, Y. Zhang, S. Sriram, K. Kalantar-Zadeh, S. Lee, R. Hillenbrand and Q. Bao, In-plane anisotropic and ultra-low-loss polaritons in a natural van der Waals crystal, Nature 562, 557-562 (2018).
- ⁴⁶ P.-Y. Chuang, S.-H. Su, C.-W. Chong, Y.-F. Chen, Y.- H. Chou, J.-C.-A. Huang, W.-C. Chen, C.-M. Cheng, K.- D. Tsuei, C.-H. Wang, Y.-W. Yang, Y.-F. Liao, S.-C. Weng, J.-F. Lee, Y.-K. Lan, S.-L. Chang, C.- H. Lee, C.-K. Yang, H.- L. Suh, Y.-C. Wu, Anti-site defect effect on the electronic structure of a Bi₂ Te₃ topological insulator, RSC Adv. 8, 423-428 (2018).
- ⁴⁷ A. Levchuk , Wilk, G. Vaudel , F. Labbé , B. Arnaud, K. Balin, J. Szade , P. Ruello , and V. Juvé, Coherent acoustic phonons generated by ultrashort terahertz pulses in nanofilms of metals and topological insulators, Phys. Rev. B 101, 180102(R) (2020).
- ⁴⁸ R. Mankowski, M. Först and A. Cavalleri, Non-equilibrium control of complex solids by nonlinear phononics, Rep. Prog. Phys. **79**, 064503 (2016).